THE VELOCITY ANISOTROPY OF DISTANT MILKY WAY HALO STARS FROM *HUBBLE SPACE TELESCOPE* PROPER MOTIONS

A.J. DEASON[1,3], R.P. VAN DER MAREL[2], P. GUHATHAKURTA[1], S.T. SOHN[2], T.M. BROWN[2]
(Dated: February 14, 2013)
Draft version February 14, 2013

ABSTRACT

Based on long baseline (5–7 years) multi-epoch *HST*/ACS photometry, used previously to measure the proper motion of M31, we present the proper motions (PMs) of 13 main-sequence Milky Way halo stars. The sample lies at an average distance of $r \simeq 24$ kpc from the Galactic center, with a root-mean-square spread of 6 kpc. At this distance, the median PM accuracy is 5 km s^{-1}. We devise a maximum likelihood routine to determine the tangential velocity ellipsoid of the stellar halo. The velocity second moments in the directions of the Galactic (l, b) system are $\langle v_l^2 \rangle^{1/2} = 123^{+29}_{-23}$ km s^{-1}, and $\langle v_b^2 \rangle^{1/2} = 83^{+24}_{-16}$ km s^{-1}. We combine these results with the known line-of-sight second moment, $\langle v_{\rm los}^2 \rangle^{1/2} = 105 \pm 5$ km s^{-1}, at this $\langle r \rangle$ to study the velocity anisotropy of the halo. We find approximate isotropy between the radial and tangential velocity distributions, with anisotropy parameter $\beta = 0.0^{+0.2}_{-0.4}$. Our results suggest that the stellar halo velocity anisotropy out to $r \sim 30$ kpc is less radially biased than solar neighborhood measurements. This is opposite to what is expected from violent relaxation, and may indicate the presence of a shell-type structure at $r \sim 24$ kpc. With additional multi-epoch *HST* data, the method presented here has the ability to measure the transverse kinematics of the halo for more stars, and to larger distances. This can yield new improved constraints on the stellar halo formation mechanism, and the mass of the Milky Way.

Subject headings:

1. INTRODUCTION

The oldest, and most metal-poor stars in our Galaxy reside in the stellar halo; a diffuse envelope of stars extending out to $r \sim 100$ kpc. The orbital timescales of these halo stars are very long compared to the age of the Galaxy, thus the phase-space structure of the stellar halo is intimately linked to its accretion history. Furthermore, the extreme radial extent of halo stars, well-beyond the baryonic center of our Galaxy, makes them excellent tracers of the dark matter halo.

Stars diffuse more quickly in configuration space as opposed to angular momentum space, so often the velocity structure of stellar halo stars provides the strongest link to their initial conditions. Global kinematic properties, such as the relative pressure between tangential and radial velocity components, otherwise known as the velocity anisotropy, can provide important insight into the formation of the stellar halo. For example, most models of violent relaxation (e.g. Diemand et al. 2004; Bullock & Johnston 2005; Sales et al. 2007), predict an increasingly radially biased velocity ellipsoid with distance. Local studies, limited to heliocentric distances $D \lesssim 10$ kpc, have utilized full three-dimensional (3D) kinematics of halo stars and find a strongly radially biased velocity anisotropy with $\beta = 1 - \langle v_t^2 \rangle / 2 \langle v_r^2 \rangle \sim 0.5 - 0.7$ (Chiba & Beers 2000; Gould 2003; Kepley et al. 2007; Smith et al. 2009; Bond et al. 2010; Carollo et al. 2010).

Beyond $D \gtrsim 10$ kpc, we are limited to one velocity component: the line-of-sight (LOS) velocity. At large distances, where $D \gg R_0$, the LOS velocity is almost identical to the radial velocity component, and hence we have a very poor handle on the tangential motion of halo stars. Despite this shortcoming, several studies have used large samples of halo stars, widely distributed over the sky, to tease out the halo velocity ellipsoid beyond $D \sim 10$ kpc. Sirko et al. (2004) modeled the LOS velocities of $N \sim 1000$ blue horizontal branch stars (BHB) selected from the Sloan Digital Sky Survey (SDSS) data release 4 (DR4) ranging from $10 \lesssim D/{\rm kpc} \lesssim 30$, and found a velocity ellipsoid with $\beta \simeq -0.1 \pm 0.2$, which is consistent with isotropy. More recently, Deason et al. (2012a) used $N \sim 2000$ BHB stars selected from SDSS DR8 between $20 \lesssim D/{\rm kpc} \lesssim 40$, to simultaneously derive the velocity anisotropy and mass profile of the Galaxy; they found a radially biased velocity anisotropy with $\beta \sim 0.5$. Finally, Kafle et al. (2012) analyzed the SDSS DR8 BHB sample (Xue et al. (2011)), and found, by dividing the sample into ~ 15 radial bins, that the anisotropy profile shows a sharp decline at $r \sim 17$ kpc to $\beta \sim -1$ and is radially biased (with $\beta \sim 0.5$) either side of this apparent dip (see also Samurović & Lalović 2011).

These observations point to a fairly complex velocity anisotropy profile at large distances, which is likely affected by substructure in the stellar halo. Unfortunately, analyses using only LOS velocities require modeling assumptions regarding the underlying potential, and it is not obvious how such systematics may bias the results. Clearly, in the ideal case, one would like to *directly measure* the tangential motions of halo stars. This is a daunting task at large distances in the halo; at $D \sim 10 - -100$ kpc, a tangential velocity of $V_t \sim 100$ km s^{-1} corresponds to a proper motion (PM) on the sky of $\mu \sim 2 - -0.2$ mas yr^{-1}. This requires an astrometric accuracy that is un-feasible for current stellar PM surveys.

The *Hubble Space Telescope* (*HST*) has unparalleled astrometric capabilities; the displacement of stars over time relative to a stationary background source can be used to produce very accurate PMs. Quasi-stellar objects (QSOs) have conventionally been used as reference sources in *HST* PM stud-

[1] Department of Astronomy and Astrophysics, University of California Santa Cruz, Santa Cruz, CA 95064, USA; alis@ucolick.org
[2] Hubble Fellow
[3] Space Telescope Science Institute, 3700 San Martin Drive, Baltimore, MD 21218, USA
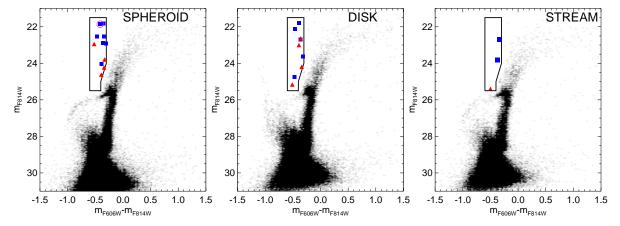
Figure 1. Color–magnitude diagrams (CMDs) of the three *HST*/ACS M31 fields (Spheroid, Disk and Stream), using the photometry from Brown et al. (2009). The black box indicates our selection of candidate foreground Milky Way halo stars. The symbols indicate the stars in each FOV which fall into our CMD selection box (11 in Spheroid, 9 in Disk and 3 in Stream). Blue squares are Milky Way halo stars, red triangles are M31 stars, and a possible Milky Way disk star is highlighted with a magenta circle (see Section 2.3).

ies (e.g. Kallivayalil et al. 2006a; Kallivayalil et al. 2006b; Piatek et al. 2008). In addition, distant background galaxies can also be used as stationary reference sources. The advantage of background galaxies is that there are many more of them over the *HST* field-of-view, therefore a $\sqrt{N}$ averaging advantage means that they can potentially yield more accurate PM measurements. Galaxy positions can be difficult to measure (compared with QSOs), but Mahmud & Anderson (2008) have recently developed a template-fitting technique to measure accurate positions of background galaxies. This technique has been extended by (Sohn et al. 2012a,b) to measure accurate PMs of local group galaxies using multi-epoch *HST* photometry. This work has yielded unprecedented PM accuracy (~ 0.01 mas yr^{-1}) and has been used to derive the tangential motion of M31, located at a distance of ~ 770 kpc, and by extension, the total mass of the local group (Sohn et al. 2012a; van der Marel et al. 2012a; van der Marel et al. 2012b)

In this study, we make use of the unparalleled PM accuracy achieved by Sohn et al. (2012a), to extract the PMs of *individual halo stars* in the foreground of these *HST*/ACS fields. The *HST* fields are small, but deep, which allows us to study foreground main-sequence (MS) halo stars. This is in contrast to spectroscopic studies, which cannot go deep enough to study this dominant stellar halo population. For the first time, we are able to directly measure the tangential motions of distant, field halo stars.

The paper is arranged as follows. In Section 2 we describe the multi-epoch *HST*/ACS imaging, and the techniques used to extract PMs of halo stars in these fields. In Section 3 we describe our analysis of the halo stars, and outline our maximum likelihood routine used to determine the halo velocity ellipsoid. Section 4 describes our results, and in Section 5 we discuss the implications of our derived halo velocity anisotropy. Finally, we summarize our main findings in Section 6.

2. *HST* DATA

The data employed in our analysis come from three *HST* observing programs: GO-9453, GO-10265 (PI: T.Brown), and GO-11684 (PI: R.P. van der Marel). Programs GO-9453 and GO-10265 obtained deep optical imaging of three fields in M31 (Spheroid, Disk and Stream: see Figure 1) in two filters (F606W and F814W) using *HST* ACS/WFC, with the primary goal of measuring the star formation history in

these fields. The observations and data reduction are described in Brown et al. (2006), and point source catalogs were distributed in Brown et al. (2009). Program GO-11684 reobserved these fields using *HST* ACS/WFC and WFC3/UVIS in order to measure the proper motions of their stars and M31 itself. These data provides five to seven year baselines with respect to the pre-existing first-epoch data. The second-epoch observations, data reduction, and determination of proper motions are described in Sohn et al. (2012a) (and see below).

2.1. *Proper Motions*

During the course of the Sohn et al. (2012a) M31 PM study, PM catalogs for *individual* stars in the three *HST* fields were created. As the M31 stars were used to align first- and second-epoch data in the Sohn et al. (2012a) study, these PMs are measured relative to the M31 stars. To obtain absolute PMs, we added the mean absolute PMs of the M31 stars for each field. For this we used the values reported by Sohn et al. (2012a), as determined with respect to stationary background galaxies. The PM errors were calculated based on the positional repeatability seen in the multiple first-epoch ACS/WFC measurements. We adopt similar errors for WFC3/UVIS as for ACS/WFC, which may be a slight overestimate since the WFC3/UVIS pixel scale is smaller.

In the following section we select potential foreground Milky Way halo stars in the three *HST*/ACS fields. The proper motions of these stars are then extracted by cross-matching with the Sohn et al. (2012a) catalog of individual star PM measurements. In the magnitude range under consideration ($21.5 \lesssim m_{F814W} \lesssim 25.5$; see below), the average uncertainty in the proper motion measurements is $\sigma_\mu \sim 0.05$ mas yr^{-1}. The corresponding velocity error depends on the distance, but for example is only 5 km s^{-1} at $D = 20$ kpc. This is considerably more accurate than previous proper motion measurements of individual stars in the halo (with $\sigma_\mu \sim 1 - -4$ mas yr^{-1}; see e.g. Munn et al. 2004; Casetti-Dinescu et al. 2006; Bramich et al. 2008)

2.2. *Selection of Foreground Milky Way Halo Stars*

We select candidate foreground Milky Way halo stars using the color-magnitude diagrams (CMDs) of the *HST*/ACS M31 fields. The main-sequence turn-off (MSTO) for Milky Way halo stars is located at brighter (apparent) magnitudes

Field	RA (J2000)	DEC (J2000)	m_{F814W}	m_{F606W}	μ_l [mas yr^{-1}]	μ_b [mas yr^{-1}]	Class	Ref
Spheroid								
	00:46:00.25	+40:41:37.88	24.05	23.66	-0.09 ± 0.05	-1.47 ± 0.06	Halo	
	00:46:01.47	+40:41:35.53	21.86	21.45	-1.96 ± 0.04	-2.08 ± 0.04	MW Disk?	
	00:46:03.79	+40:41:22.81	22.53	22.19	1.36 ± 0.02	-1.33 ± 0.02	Halo	
	00:46:03.67	+40:41:56.60	22.88	22.52	2.12 ± 0.03	-0.82 ± 0.02	Halo	
	00:46:04.91	+40:41:55.88	23.79	23.46	-0.19 ± 0.04	-0.42 ± 0.03	M31	V60 (B04)
	00:46:04.92	+40:42:47.16	24.23	23.89	0.21 ± 0.03	-0.28 ± 0.03	M31	
	00:46:06.41	+40:42:15.07	22.53	22.06	1.45 ± 0.02	-0.90 ± 0.02	Halo	
	00:46:05.14	+40:43:37.19	21.82	21.47	3.91 ± 0.02	-1.59 ± 0.02	Halo	
	00:46:10.05	+40:43:06.01	22.94	22.42	0.19 ± 0.03	$+0.22 \pm 0.03$	M31	V118 (B04; K06)
	00:46:12.92	+40:41:22.51	22.92	22.61	1.88 ± 0.06	-2.83 ± 0.06	Halo	
	00:46:12.06	+40:42:25.05	24.62	24.23	-0.06 ± 0.06	$+0.12 \pm 0.05$	M31	
Disk								
	00:49:04.66	+42:44:33.36	25.16	24.65	$+0.06 \pm 0.11$	$+0.01 \pm 0.10$	M31	V5719 (J11)
	00:49:08.91	+42:44:13.62	21.79	21.40	-0.59 ± 0.03	-1.50 ± 0.04	Halo	
	00:49:08.30	+42:44:50.44	22.12	21.66	$+1.03 \pm 0.04$	-0.78 ± 0.04	Halo	
	00:49:09.77	+42:44:51.02	24.19	23.85	-0.31 ± 0.06	-0.22 ± 0.07	M31	
	00:49:13.50	+42:43:36.17	22.71	22.35	-0.71 ± 0.07	-0.67 ± 0.08	Halo	
	00:49:11.84	+42:44:25.08	23.00	22.61	-0.20 ± 0.04	-0.08 ± 0.04	M31	
	00:49:10.54	+42:45:25.94	22.64	22.28	$+0.16 \pm 0.05$	$+0.29 \pm 0.04$	M31	V13779 (J11)
	00:49:13.38	+42:45:56.93	23.62	23.30	$+2.16 \pm 0.05$	-0.40 ± 0.06	Halo	
	00:49:13.69	+42:45:52.07	24.76	24.29	$+0.64 \pm 0.07$	$+0.58 \pm 0.06$	Halo	
Stream								
	00:44:15.06	+39:48:42.50	25.38	24.88	-0.18 ± 0.08	$+0.55 \pm 0.08$	M31	
	00:44:26.44	+39:47:33.43	22.69	22.35	$+0.00 \pm 0.06$	-1.85 ± 0.06	Halo	
	00:44:23.93	+39:46:26.25	23.83	23.46	-0.43 ± 0.05	-1.13 ± 0.07	Halo	

Table 1
The properties of candidate foreground halo stars selected from the M31 CMDs. We give the right ascension (RA) and declination (DEC), *HST*/ACS STMAG magnitudes, Galactic PMs and designated class (Halo, MW Disk or M31 star). The RA, DEC and magnitudes come from Brown et al. (2009), and the proper motions derive from the study by Sohn et al. (2012a). Variables stars in M31 identified by Brown et al. 2004 (B04) and Jeffery et al. 2011 (J11) are indicated. One of these stars, V116, was also identified as an M31 member by Kalirai et al. (2006) as part of the Spectroscopic and Photometric Landscape of Andromeda's Stellar Halo (SPLASH) survey.

than the M31 MSTO, but at similar colors blue-ward of $m_{F606W} - m_{F814W} \sim -0.3$. In Figure 1, our color-magnitude selection box is shown on the CMDs of the three M31 fields. We target halo stars in a sparsely populated region of the CMD, where we expect the least contamination from Milky Way disk stars and M31 stars. We select 13, 9 and 3 stars from the Spheroid, Disk and Stream fields respectively, giving a total of 23 candidate halo stars from the three M31 fields. The extracted PMs and *HST*/ACS STMAG magnitudes are given in Table 1.

2.3. *Comparison with Besançon Galaxy model*

In Figure 2 we compare our CMD halo star selection with the Besançon Galaxy model (Robin et al. 2003). We select stars from this model in a 1 deg^2 field-of-view (FOV) centered on M31. We convert Johnson-Cousins *UBVRI* photometry to *HST*/ACS STMAG using the relations given by Sirianni et al. (2005). The stars inside our color-magnitude selection box are predominantly halo MS stars, and a small fraction (7 %) are disk stars. Most of these disk stars are intrinsically faint white dwarfs, which have similar (blue) colors to MSTO stars. Note that if we scale this 1 deg^2 FOV to the *HST*/ACS FOV then the Besançon model predicts $N \sim 5$ halo stars per *HST* pointing. Our sample of $N = 23$ stars from three pointings is slightly higher than this prediction; this is due to contamination by M31 stars in our sample, which we now discuss.

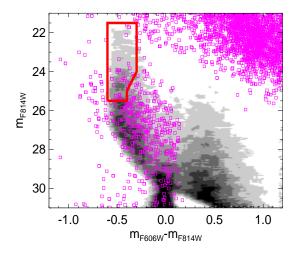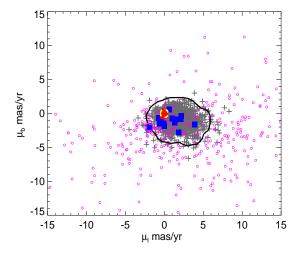Figure 3 shows the Galactic proper motion components of

Figure 2. A CMD for stars in the Besançon Galaxy model. The FOV is 1 deg^2 and is centered on M31. The black/gray shaded regions indicate halo stars and the magenta squares indicate disk stars (only 25% of disk stars are shown for clarity). Within our selection box, 7% of the foreground stars are disk stars.

the Besançon Galaxy model stars which lie within our color-magnitude selection box. The gray crosses are halo stars and the magenta circles are disk stars. The disk stars have a much
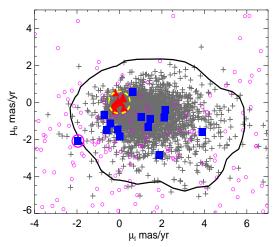
Figure 3. Proper motions (PMs) of stars in the Besançon model in Galactic coordinates (μ_l, μ_b). The stars shown cover a 1 deg^2 FOV centered on M31, and fall in the CMD selection box given in Figure 1. The gray crosses are halo stars and the magenta circles are disk stars. The blue squares show the PMs of stars selected from the M31 CMDs in Figure 1. The distribution of PMs is offset in the positive μ_l direction; this is due to the reflex motion of the Sun. There is a concentration of (9) stars with zero PM, consistent with the net PM of M31 (see Sohn et al. 2012a; van der Marel et al. 2012a). These stars are highlighted with red triangles, and the dashed-yellow circle shows the region in PM space consistent with M31 stars. The black contour encompasses 99% of the halo population in the Besançon model. Outside of this contour, the bias caused by including high PM disk stars becomes non-negligible. The bottom panel is a zoom-in of the top panel.

higher spread in PM than the halo stars. This is because the stars belonging to the Milky Way disk are much closer than the halo stars, so they tend to have much larger proper motions. The black contour indicates the PM region containing 99% of the halo stars. Within this region there is a very small amount of disk contamination ($\sim 1\%$), and the low PM disk stars have a negligible effect on our analysis described in Section 3 (see discussion in Section 4.2.3). The blue squares (and red triangles) show the PMs of the 23 stars selected from the *HST*/ACS images. Encouragingly, the distribution of PMs closely resembles the halo population of the Besançon model.

The dashed yellow circle indicates the region in PM space

consistent with the net PM of M31 (($\mu_{l,M31}, \mu_{b,M31}$) = $(0.04, -0.03) \pm 0.01$ mas yr^{-1}; Sohn et al. 2012a[4]). Note that this region in PM space has a radius of ~ 0.5 mas yr^{-1}. There are $N = 9$ stars in our sample that lie within this region, which are highlighted by red triangles. Given the uncertainties in our proper motion measurements and the internal velocity dispersion in the M31 fields ($V_{int} \sim 125$ km s^{-1}, see van der Marel et al. 2012a), we find that these nine stars are typically within 3–4 σ of the net motion of M31. In the following analysis we excise these stars from our sample as they are, presumably, horizontal branch, asymptotic giant branch and/or variable M31 stars. In fact, four of these stars have been identified as variable stars in M31 from independent studies (Brown et al. 2004; Jeffery et al. 2011).

Of the remaining $N = 14$ stars, one lies outside the 99% contour of the Besançon model, this star is highlighted with a magenta circle. Given the prediction of 7% disk contamination from the Besançon model, it's likely that we may have ~ 1 disk star in our sample of 14 stars, and the location of this star in PM space makes it the most probable candidate. In our analysis below, we only consider stars within the 99% contour defined by the Besançon model, and so we do not include this star. However, we note that these two biases in PM space (due to M31 stars and disk stars) are *fully accounted for* in our analysis. Furthermore, we verify that a slightly different choice of contour, which includes this possible disk star, does not change the final velocity ellipsoid results by more than ~ 15 km s^{-1}, which is less than our statistical uncertainties (~ 30 km s^{-1}). In the following section we outline how we model the tangential velocity components of the remaining $N = 13$ halo stars.

3. ANALYSIS

3.1. *Distance Calibration*

The tangential motion of the halo stars depends on their PM and distance: $v_t = 4.74047 \mu D$. Here, the PM is in mas yr^{-1} and the heliocentric distance is in kpc.

The large spread in absolute magnitude of stars near the MSTO means that we cannot determine an accurate distance to individual halo stars. Therefore, we cannot measure the velocity ellipsoid directly, despite the fact that we have very accurate PMs. However, we can determine a probability distribution function (pdf) of halo star distances, based on a suitably chosen model for the star formation history and 3D density distribution of the halo (both of which have been well constrained by existing studies). This allows a statistical determination of velocity ellipsoid, without knowing the actual 3D velocities of individual stars.

We calibrate the pdf of halo star absolute magnitudes via a two step process: First, we use suitably chosen isochrones to describe the distribution of absolute magnitudes as a function of color. Second, we translate this distribution into a continuous, analytic pdf that can be used in a maximum likelihood routine (see Section 3.2).

3.1.1. *Weighted Isochrones*

We use the VandenBerg et al. (2006) isochrones, calibrated for *HST*/ACS STMAG photometry (Brown et al. 2005), to model the absolute magnitudes of our selected halo stars.

---

[4] Sohn et al. (2012a) gave values in the (W,N) frame. However, at the location of M31, the (W,N) and (l,b) coordinate frame are aligned to within 2 degrees.
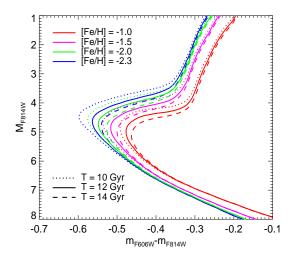
Figure 4. VandenBerg et al. (2006) isochrones in the *HST*/ACS STMAG system. Metallicities in the range $-2.3 \leq \text{[Fe/H]} \leq -1.0$ are shown by the colored lines, and ages between $10 \leq T/\text{Gyr} \leq 14$ are shown by different line styles. All these isochrones have an alpha to iron-peak element ratio $[\alpha/\text{Fe}] = 0.3$.

In Figure 4 we show isochrones for a range of metallicities ($-2.3 \leq \text{[Fe/H]} \leq -1.0$) and ages ($10 \leq T/\text{Gyr} \leq 14$) applicable for a halo population. In the color range of our sample, $m_{\text{F606W}} - m_{\text{F814W}} < -0.3$, the halo stars are close to the MSTO, but they can also lie at fainter magnitudes on the MS, or brighter magnitudes on the red giant branch (RGB). Thus, the absolute magnitudes can range from $3 \lesssim M_{\text{F814W}} \lesssim 7.5$, and our sample of halo stars potentially spans a distance range, $10 \lesssim D/\text{kpc} \lesssim 100$.

We model the absolute magnitudes of the halo stars as a function of color, and apply three weighting factors to the isochrones:

- Initial-mass-function (IMF) weight: We assume a Salpeter IMF and weight the contribution from different mass stars accordingly. Low mass MS stars thus have higher weight than higher mass RGB stars.

- Metallicity weight: We assume the halo population has a Gaussian distribution of metallicities with mean $\text{[Fe/H]} = -1.9$ and dispersion $\sigma = 0.5$ (see e.g. Xue et al. 2008). We assume the metallicity distribution is constant with radius; this is in good agreement with recent studies which find no significant metallicity gradient in the stellar halo (Ma Z. et al. in preparation).

- Age weight: We weight the different age isochrones by assuming a Gaussian distribution of ages with mean $\langle T \rangle = 12$ Gyr and dispersion $\sigma = 2$ Gyr (see e.g. Kalirai 2012).

In Fig. 5 we show the absolute magnitude distribution in six color bins, weighted by IMF, metallicity and age. The dashed blue line shows a double-Gaussian fit to each color bin. At redder colors the distribution of absolute magnitudes separates into the MS and RGB populations, while at bluer colors the populations merge into the MSTO.

3.1.2. *Analytic absolute magnitude calibration*

In Figure 6 we show the parameters from the double-Gaussian fits (amplitude, mean and sigma) for both the RGB

and MS populations as a function of color. The dashed red lines are polynomial (second or third order) fits to the relations. We use these polynomial relations to define a continuous, double-Gaussian pdf for absolute magnitude as a function of color:

$$G(M_{\text{F814W}}|m_{\text{F606W}} - m_{\text{F814W}}) = G_1(A_1, M_1, \sigma_1, M_{\text{F814W}}) + G_2(A_2, M_2, \sigma_2, M_{\text{F814W}}) \quad (1)$$

where, $G(A, M, \sigma, x) = A \exp\left[-(x-M)^2/(2\sigma^2)\right]$, and A, M and σ (amplitude, mean and sigma) are polynomial functions of $m_{\text{F606W}} - m_{\text{F814W}}$ color.

The red squares in Figure 5. show the absolute magnitude distributions reproduced by our analytic model. These are in good agreement with the (non-analytic) distributions derived from the weighted isochrones.

In the following section, our absolute magnitude pdf is used in a maximum likelihood routine to determine the tangential components of the halo velocity ellipsoid.

3.2. *Maximum Likelihood Method*

In this section, we outline the maximum likelihood method used to derive the tangential velocity ellipsoid components of the Milky Way halo. We assume that the velocity distribution in the plane of the sky follows a Gaussian distribution, with constant ($\sigma_l, \sigma_b, v_{l,0}, v_{b,0}$) over the radial range spanned by our data:

$$F_v(v_l, v_b) \propto \exp\left[-\frac{(v_l - v_{l,0})^2}{2\sigma_l^2}\right] \exp\left[-\frac{(v_b - v_{b,0})^2}{2\sigma_b^2}\right] \quad (2)$$

In the halo, where $D \gg R_0 \simeq 8.5$ kpc, the Galactic coordinates, l, b are good approximations to the spherical coordinates, ϕ, θ respectively. For each star, there are six observables: the angular position on the sky (l, b), the PM (μ_l, μ_b), and the two photometric magnitudes ($m_{\text{F814W}}, m_{\text{F606W}}$). Observed heliocentric velocities are converted to Galactocentric ones by assuming a circular speed of 240 km s^{-1} (e.g. Reid et al. 2009; McMillan 2011; Schönrich 2012) at the position of the sun ($R_0 = 8.5$ kpc) with a solar peculiar motion $(U, V, W) = (11.1, 12.24, 7.25)$ km s^{-1} (Schönrich et al. 2010). Here, U is directed toward the Galactic center, V is positive in the direction of Galactic rotation and W is positive towards the North Galactic Pole. In the direction of M31, the velocity of the sun projects to: $(v_l, v_b) = (-139.5, 83.7)$ km s^{-1}.

The halo pdf at fixed $m_{\text{F606W}} - m_{\text{F814W}}$ color, in increments of absolute magnitude, apparent magnitude, Galactic PM and solid angle, $F(y)$, where y is defined as $y = y(M_{\text{F814W}}, m_{\text{F814W}}, \mu_l, \mu_b, \Omega)$, is given by:

$$F \Delta\mathbf{y} \propto F_v \rho D^5 G \Delta\mathbf{y} \quad (3)$$

Here, $D = D(M_{\text{F814W}}, m_{\text{F814W}})$ is the heliocentric distance, $F_v = F_v(D, \mu_l, \mu_b)$ is the velocity distribution function given in Equation 2, $\rho = \rho(D, l, b)$ is the density distribution of halo stars, $G = G(M_{\text{F814W}}|m_{\text{F606W}} - m_{\text{F814W}})$ is the absolute magnitude pdf defined in Equation 1 and $\Delta\mathbf{y} = \Delta M_{\text{F814W}}\Delta m_{\text{F814W}}\Delta\mu_l\Delta\mu_b\Delta\Omega$ is the volume element. We assume the halo stars follow the broken power-law density profile derived by Deason et al. (2011b), but we comment on the effect of the density profile parameterization on our results in Section 4.2.2. We marginalize over the abso-
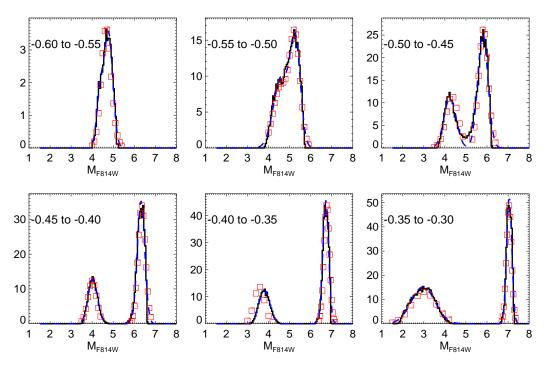
Figure 5. The M_{F814W} absolute magnitude distribution of the VandenBerg et al. (2006) isochrones in six color bins. The MSTO dominates at bluer colors, while at redder colors the MS and RGB populations separate into two distinct populations. The blue lines show double-Gaussian fits to the distributions. The red squares indicate the distributions reproduced by our analytic model (see Equation 1) in these six color bins.
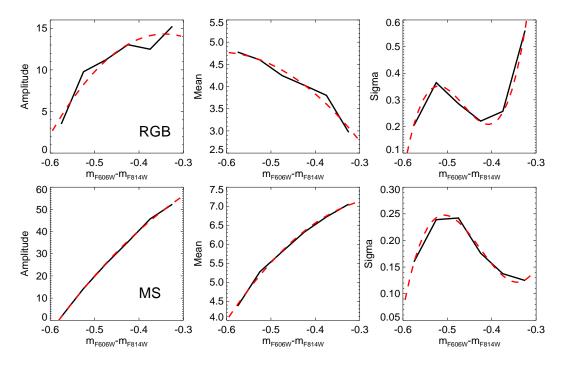

Figure 6. The Gaussian parameters (amplitude, mean and sigma), which define the RGB and MS absolute magnitude calibrations, are shown as a function of color. The dashed-red lines show continuous polynomial fits (second or third order) to the relations.
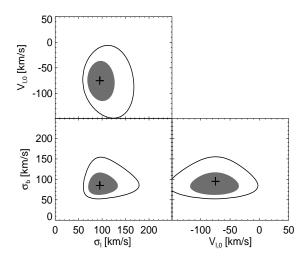
Figure 7. Likelihood contours for the halo velocity ellipsoid in the plane of the sky. The shaded gray regions and solid lines show the 1σ and 2σ confidence intervals, and the black crosses indicate the maximum likelihood parameters.

lute magnitude coordinate, $\bar{F} = \int F \, dM_{F814W}$, and define the likelihood function:

$$L = \prod \bar{F}(\sigma_l, \sigma_b, v_{l,0}, v_{b,0}, \mathbf{x}) \qquad (4)$$

Here, $\mathbf{x}$ denotes the observables ($m_{F814W}, m_{F606W} - m_{F814W}, \mu_l, \mu_b, l, b$), and $\sigma_l, \sigma_b, v_{l,0}, v_{b,0}$ are free parameters. We use a brute force grid method to find the maximum likelihood parameters. The net motion in Galactic latitude, $v_{b,0}$, is set to zero, while we allow for net motion in Galactic longitude, $v_{l,0} \sim -v_{\phi,0}$, which approximates the net rotational velocity of the halo.

The kinematical biases that we have introduced (see Figure 3) are accounted for through a renormalization of the likelihood function over the region in observable-space that passes our cuts. In Equation 4, $\bar{F}(p, \mathbf{x})$ is the normalized probability that a star exists at observables $\mathbf{x}$, given model parameters $p = (\sigma_l, \sigma_b, v_{l,0}, v_{b,0})$. We define $F_{sel}(\mathbf{x})$ as our selection function, which states the probability that a star with observables $\mathbf{x}$ is in our sample. Thus, $F_{sel}(\mathbf{x})$ is 1 or 0, depending on our adopted cuts. The normalized probability that a star is found in our sample, at observables $\mathbf{x}$, given model parameters p is given by: $\bar{F}(p, \mathbf{x})F_{sel}(\mathbf{x})/N(p)$. Here, $N(p) = \int_{\mathbf{x}_c} \bar{F}(p, \mathbf{x})F_{sel}(\mathbf{x})$ is the normalization factor, and $\mathbf{x}_c$ denotes the region in $\mathbf{x}$-space that passes our selection cuts. We calculate these integrals numerically. This procedure reduces the likelihood to:

$$L = \prod \frac{\bar{F}(p, \mathbf{x})}{N(p)} \qquad (5)$$

since, by definition, $F_{sel}(\mathbf{x}_i) = 1$ for any star $i = 1, ..., N$ that makes it into our sample.

In the following Section, we discuss the results of applying this maximum likelihood algorithm to our sample of halo stars.

4. HALO VELOCITY ANISOTROPY

4.1. *Results*

In Figure 7 we show the results of our maximum likelihood analysis (see also Table 2). The resulting velocity

moments[5] in the plane of the sky are: $\sigma_b = 83^{+24}_{-16}$ km s^{-1}, $\sigma_l = 94^{+28}_{-18}$ km s^{-1}, and $v_{l,0} = -75^{+28}_{-29}$ km s^{-1}. We calculate the mean and root-mean-square spread of the halo star distances using the pdf of our favored parameters, e.g. $\langle D \rangle = 1/N \sum_i^N \int F_{ml} D \, dD$, where F_{ml} denotes the pdf assuming our maximum likelihood parameters. We find $\langle D \rangle = 19 \pm 1$ kpc and $\sigma_D = 6 \pm 2$ kpc. In Galactocentric radii, this corresponds to $r \sim 24$ kpc.

Our maximum likelihood velocity ellipsoid quantities are converted into a spherical polar coordinate system using a Monte Carlo method. We generate stars which follow the stellar halo density profile (Deason et al. 2011b), and assign v_l and v_b velocity distributions drawn from our likelihood constraints on σ_l, σ_b and $v_{l,0}$. In the approximate distance range of our sample, $10 \lesssim D/\text{kpc} \lesssim 30$, the LOS velocity distribution of stellar halo stars, is approximately Gaussian with $\sigma_{los} = 105 \pm 5$ km s^{-1} (see Sirko et al. 2004; Xue et al. 2008; Brown et al. 2010); we apply this LOS velocity distribution to our Monte Carlo samples. The v_r, v_θ, v_ϕ velocity components are then calculated from the generated star positions and v_{los}, v_b, v_l velocities. In Table 2 we show the resulting velocity ellipsoids in spherical polar coordinates. As expected, the v_θ, v_ϕ velocity distributions closely follow the v_b, v_l coordinates.

To calculate the velocity anisotropy we consider the ratio of tangential and radial pressures, i.e. $\langle V_t^2 \rangle / \langle V_r^2 \rangle$, where $\langle V_t^2 \rangle = \sigma_\phi^2 + \langle v_\phi \rangle^2 + \sigma_\theta^2$. The resulting velocity anisotropy suggests isotropic velocity pressure, with $\langle V_t^2 \rangle / \langle V_r^2 \rangle = 1.0^{+0.2}_{-0.1}$ or $\beta = 0.0^{+0.2}_{-0.4}$, this is in contrast to the highly radial values found in the solar neighborhood: $\beta \sim 0.7$ or $(\sigma_r, \sigma_\phi, \sigma_\theta) \sim (140, 80, 80)$ km s^{-1} (Smith et al. 2009; Bond et al. 2010; Carollo et al. 2010). However, several studies estimating velocity anisotropy from LOS velocity alone, in the distance range, $10 \lesssim D/\text{kpc} \lesssim 30$, also find a *more tangential* velocity ellipsoid than the solar neighborhood (Sirko et al. 2004; Deason et al. 2011a; Kafle et al. 2012). We note that a significant contribution to the tangential pressure comes from angular momentum, as $v_\phi \sim 70$ km s^{-1}. In the following section, we discuss some potential systematics which could bias our results. Encouragingly, we find that systematics play a minor role in the total error budget.

4.2. *Possible Systematics*

4.2.1. *Stellar Isochrones*

In Section 3.1 we use the VandenBerg et al. (2006) isochrones to calibrate our halo star distances. This analysis relies on our assumptions of metallicity and age for the stellar halo. We adopt isochrones applicable to an old ($T = 12 \pm 2$ Gyr) and metal-poor ([Fe/H] $= -1.9 \pm 0.5$) stellar population, but it is worth remarking how these assumptions may affect our results. Older and/or more metal-rich populations have fainter absolute magnitudes and hence higher weight is given to smaller distances in our analysis (and therefore, lower velocities). For example, the isochrones in the Besançon model assume a similar halo metallicity distribution ([Fe/H] $= -1.78 \pm 0.5$), but assume an older 14 Gyr age population. If we adopt this absolute magnitude calibration in our likelihood analysis, then our velocity ellipsoid parameters are decreased by $(\Delta\sigma_l, \Delta\sigma_b) = (-3, -5)$ km s^{-1}. Sim-

---

[5] We also applied our likelihood method setting $\langle v_l \rangle \sim -\langle v_\phi \rangle = 0$. This yields higher σ_ϕ, but the same answer for $\sigma_\phi^2 + \langle v_\phi \rangle^2$

Velocity Ellipsoid [km s^{-1}]			
Galactic	$\langle v_{\rm los}^2 \rangle^{1/2} = 105^{+5}_{-5}$	$\langle v_b^2 \rangle^{1/2} = 83^{+24}_{-16}$	$\langle v_l^2 \rangle^{1/2} = 123^{+29}_{-23}$	$\langle v_l \rangle = -75^{+28}_{-29}$
Spherical polars	$\langle v_r^2 \rangle^{1/2} = 107^{+6}_{-5}$	$\langle v_\theta^2 \rangle^{1/2} = 86^{+22}_{-16}$	$\langle v_\phi^2 \rangle^{1/2} = 121^{+28}_{-21}$	$\langle v_\phi \rangle = 73^{+28}_{-27}$
Velocity Anisotropy			
$\beta = 0.0^{+0.2}_{-0.4}$	$\sqrt{\frac{\langle v_t^2 \rangle}{\langle v_r^2 \rangle}} = 1.0^{+0.2}_{-0.1}$	$\sqrt{\frac{\langle v_\phi^2 \rangle}{\langle v_\theta^2 \rangle}} = 1.4^{+0.4}_{-0.3}$	
Position			
$l = 121°$	$b = -21°$	$\langle D \rangle = 19 \pm 1 \pm 6$ kpc	$\langle r \rangle = 24 \pm 1 \pm 6$ kpc

Table 2

Summary of our main results. We give the velocity ellipsoid in Galactic and spherical coordinate systems and the resulting velocity anisotropy. Note, the LOS velocity dispersion is estimated by previous studies in the literature (see text for more details). We also give the approximate location of our three *HST* fields in the plane of the sky, as well as the average heliocentric and Galactocentric distances for our sample. For the latter quantities we list two uncertainties, the first being the error in the mean, and the second being the root-mean-square spread of the sample.

ilarly, younger and/or metal-poorer populations will slightly increase the estimated velocity dispersions. We find that variations in the mean metallicity and/or age by 0.5 dex and 2 Gyr respectively, at most can change the velocity dispersions by ~ 10 km s^{-1}, which is well below our observational random errors. We note that more substantial variations require significant changes in metallicity and/or age, contrary to observational constraints and theoretical predictions.

4.2.2. *Density Profile*

We adopt a broken power-law stellar halo density profile, with halo flattening $q = 0.59$, ellipsoidal break radius $r_b = 27$ kpc, and inner and outer power-laws, $\alpha_{\rm in} = 2.3$, $\alpha_{\rm out} = 4.6$ (Deason et al. 2011b). The uncertainty in the halo star distances means that the density profile component of the pdf could potentially affect our derived velocity ellipsoid. For example, a shallower density profile will give higher weight to larger distances (and hence higher velocities), than a steeper density profile, and the derived velocity dispersions will therefore be higher. Encouragingly, recent studies show general agreement on the form of the stellar halo density profile out to 50 kpc (see e.g. Watkins et al. 2009; Sesar et al. 2011; Deason et al. 2011b). For example, if we instead adopt the density profile derived by Sesar et al. (2011) ($q = 0.7$, $r_b = 28$ kpc, $\alpha_{\rm in} = 2.6$, $\alpha_{\rm out} = 3.8$), our velocity ellipsoid values are increased by $(\Delta\sigma_l, \Delta\sigma_b) = (6, 3)$ km s^{-1}. These are very small differences relative to the statistical uncertainties in our results (~ 30 km s^{-1}). Note that a very steep halo density profile ($\alpha \gtrsim 6$) is required to significantly *decrease* our tangential velocity ellipsoid values.

We also note that the systematics primarily associated with distances, affect our estimate of $\langle V_t^2 \rangle$ more than the ellipsoid ratio $\langle V_\phi^2 \rangle / \langle V_\theta^2 \rangle$. This is because any systematic in our distance calibration, affects both tangential components by a similar degree.

4.2.3. *Disk Contamination*

The Besançon Galaxy model predicts that the majority of stars selected from our color-magnitude cut are halo stars, but $\sim 7\%$ of the stars could belong to the Milky Way disk. Our further restriction in proper motion space (see Figure 3), reduces this level of contamination even further (to 1% in the

Besançon model). Even so, we have quantified any bias due to the remaining disk stars. We select $N = 13$ stars at random from the Besançon model using our color-magnitude and PM selection, and apply our maximum likelihood analysis. We repeat this process using $N = 13$ *pure halo stars* from the Besançon model. After 10^4 trials, we can quantify any biases due to contamination by the small number of disk stars. We find that any biases are negligible (< 5 km s^{-1}), and can be safely ignored in the current analysis. However, we note that if we apply a less restrictive contour in proper motion space (see Figure 3), then these biases can increase.

4.2.4. *Solar Motion*

In recent years, the solar motion — and in particular, the azimuthal velocity of the Sun — has come under renewed scrutiny. There has been some debate over whether the circular velocity at the position of the Sun ($R_0 = 8.5$ kpc) is close to the IAU-recommended value, $V_c = 220$ km s^{-1}, or if it needs to be revised upwards to $V_c = 240$ km s^{-1} (e.g. Reid et al. 2009; McMillan 2011; Schönrich 2012). Recently, Bovy et al. (2012) showed that the azimuthal velocity of the sun is close to $v_\phi \sim 240$ km s^{-1}. However, the authors claim that this is due to an offset between the azimuthal velocity of the Local Standard of Rest and the local circular velocity, rather than a change in the circular velocity. In either case, the net solar motion — the quantity of importance in this study — remains uncertain.

In the context of the present study, variation of the azimuthal solar motion by ~ 20 km s^{-1} can change the projection of the solar motion in the direction of M31 by approximately $(|\Delta v_l|, |\Delta v_b|) \sim (10, 5)$ km s^{-1}. This will most notably affect our estimate of net rotation in the halo by ~ 10 km s^{-1}. Thus, even with a decrease in the Sun's rotational velocity of 20 km s^{-1}, we still find a significant signal of rotation in our sample. We note that the velocity anisotropy is largely unaffected by this translation.

5. DISCUSSION

Our measurement of an *isotropic* velocity anisotropy at $r \sim 24$ kpc, is at odds with theoretical predictions of violent relaxation, where β tends to *increase* with radius: Our result of $\beta = 0.0^{+0.2}_{-0.4}$ is lower than solar neighborhood mea-
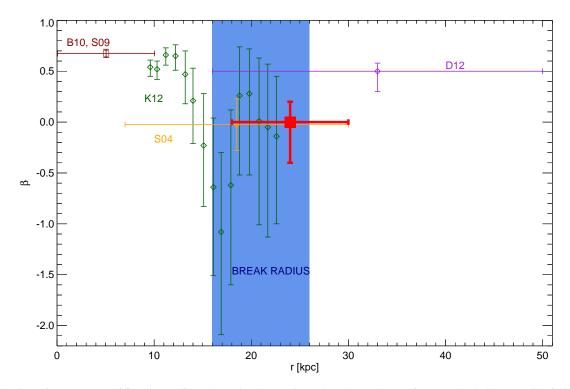
Figure 8. Velocity anisotropy as a of function radius. The colored error bars show the estimates from nearby halo stars with full 3D velocity measurements (Bond et al. 2010: B10; Smith et al. 2009: S09), and distant ($D \gtrsim 10$ kpc) halo stars with LOS velocity measurements (Sirko et al. 2004: S04; Deason et al. 2012a: D12; Kafle et al. 2012: K12). The red error bar shows our measure from $N = 13$ halo stars with PM measurements in the radial range $18 \lesssim r/\mathrm{kpc} \lesssim 30$. The blue shaded region indicates the approximate radial range of the 'break radius' in the Milky Way stellar halo ($16 \lesssim r/\mathrm{kpc} \lesssim 26$: Deason et al. 2011b)

surements by $\sim 3\sigma$. In this section, we discuss some possible explanations for this surprising result.

5.1. *Global Substructure: A Galactic Shell?*

In Figure 8 we show velocity anisotropy as a function of radius, based on various estimates from the literature. When our results are compared to solar neighborhood measures of β at smaller radii, and LOS velocity estimates at larger radii, we begin to see that the velocity anisotropy may have a 'dip' at $r \sim 20$ kpc, rather than a constant or continuous decline. Furthermore, the location of this possible dip is coincident with a break in the stellar halo density: Deason et al. (2011b) (see also Sesar et al. 2011; Watkins et al. 2009) find that the stellar halo density profile declines more rapidly beyond a break radius of $r \sim 16 - 26$ kpc. The origin of this break radius is still uncertain: Deason et al. (2013) recently suggested that the break radius in the Milky Way may be due to a shell-type structure built up from the aggregation of accreted stars at apocenter. However, Beers et al. (2012) claim that the break radius signifies a transition between two halo populations of different origin (see discussion below). In the former scenario, the kinematic signature of a shell — a predominance of tangential motion at the turn-around radius, plus a cold radial velocity dispersion — is intriguingly similar to the apparent 'dip' in velocity anisotropy that we observe. At present, the evidence for a rise again in velocity anisotropy beyond $r \sim 30$ kpc, relies solely on LOS velocities, where the derived anisotropy is intimately linked to the assumptions of the halo potential. Therefore, it is important to independently determine the tangential motion of halo stars *beyond* the break radius in order to confirm/falsify the apparent dip in anisotropy.

It is possible that some of our halo stars belong to the "TriAnd" overdensity. This structure subtends an area of at least $50° \times 60°$ in the constellations of Triangulum and Andromeda, and is located at a similar distance to our halo sample ($16 \lesssim D/\mathrm{kpc} \lesssim 25$, Rocha-Pinto et al. 2004; Majewski et al. 2004; Martin et al. 2007). The nature of TriAnd has been debated in the literature; Rocha-Pinto et al. (2004) (see also Majewski et al. 2004) propose either a bound core of a very dark matter dominated dwarf or a portion of a tidal stream, while Johnston et al. (2012) suggest that TriAnd is an apogalactian piece of a disrupted dwarf galaxy. The conclusions we draw here are most consistent with the latter interpretation.

5.2. *Stellar Halo Formation Mechanism: In-Situ Stars?*

In recent years, an additional formation mechanism for halo stars has been put forward. Studies based on hydrodynamical cosmological simulations suggests that halo stars can form *in-situ* from gas in the parent galaxy in addition to formation in external dwarf galaxies and then subsequent accretion (Zolotov et al. 2009; Font et al. 2011). McCarthy et al. (2012) showed that these in-situ stars can have significant prograde rotation and therefore increased tangential pressure support from angular momentum. Therefore, this alternative formation mechanism for halo stars could also explain the more tangentially biased halo star orbits. However, this does not explain why the orbits of halo stars in the solar neighborhood — presumably where *in-situ* stars are more dominant over accreted stars — have such strongly radial orbits.

5.3. *A Cold Stream?*

Finally, our sample of halo stars is small ($N = 13$) and covers a narrow FOV, so we cannot reject the possibility that our results are biased by local substructure. However, we do not find any obvious clustering of our sample in PM space, so it seems unlikely that the majority of our halo stars belong to a common stream. Furthermore, the agreement of our results with studies using LOS velocities in a similar radial regime but different directions on the sky, suggests that the isotropic velocity anisotropy derived here is a true global property.

5.4. *Halo Rotation*

We find a significant signal of prograde rotation in our halo sample, with $\langle v_\phi \rangle \sim 70$ km s^{-1}. As mentioned above, this signal could be due to the presence of a shell-type structure in this radial regime, or the halo could have a net rotation — perhaps due to the influence of stars born *in-situ*. Previous work on the rotation of halo populations have found contrasting results. Frenk & White (1980) and Zinn (1985) found evidence of net prograde rotation in the Milky Way globular cluster population (with $\langle v_\phi \rangle \simeq 50 - -60$ km s^{-1}). More recently, Deason et al. (2011a) find that BHB stars with [Fe/H] > -2 have a net streaming motion of $\langle v_\phi \rangle \sim 50$ km s^{-1} in a similar radial range to this study. However, Carollo et al. (2010) claim that their sample of outer ($D > 15$ kpc) halo stars have a net *retrograde* rotation with $v_\phi \sim -80$ km s^{-1} (but see Schönrich et al. 2011).

It is clear that a confused picture surrounds the rotational properties of the halo. This is something we hope to address in the future with additional *HST* fields.

5.5. *Future Work*

The above discussion illustrates the importance of measuring the radial velocity anisotropy profile in order to understand the formation mechanism of the stellar halo. We hope to extend this present study to multiple *HST* fields with long-baseline multi-epoch photometry. This will enable us to move beyond small number statistics, cover a wider area on the sky, and probe further out into the stellar halo. Studies using LOS velocity measurements rely on assumptions of the halo potential and are limited to within $r \lesssim 30 - 40$ kpc: using PMs, we can more directly measure the tangential motion of halo stars. Furthermore, the depth of the *HST* fields allows us to study MS stars; the dominant population of the stellar halo. Current spectroscopic studies and the upcoming *Gaia* mission (with magnitude limit $V < 20$) are limited to intrinsically bright halo stars, such as BHB or RGB stars, which may not be unbiased tracers.

Finally, an *independent* measure of velocity anisotropy is vital in order to derive the mass profile of our Galaxy. Recently, Deason et al. (2012b) found that the radial velocity dispersion of halo stars declines rapidly at large radii. At present, the degeneracy between tracer density, anisotropy and halo mass cannot be disentangled. However, a measure of the tangential motion of these distant halo stars will allow us to address whether or not this cold radial velocity dispersion is due to a shift in pressure from radial to tangential components. Our method, using multi-epoch *HST* images, may be the *only* way to measure velocity anisotropy at these large distances. The upcoming *Gaia* mission will measure proper motions for an unprecedented number of halo stars with $V < 20$, and will likely revolutionize our understanding of the inner stellar halo. However, even with bright halo tracers (e.g. BHB or Carbon stars), the PM accuracy of *Gaia*, $\sigma_\mu \sim 0.3$ mas yr^{-1} ($\sigma_V \sim 140$ km s^{-1} at $D \sim 100$ kpc), will be unable to accurately constrain the tangential motion of very distant halo stars.

The PM accuracies achievable with just a few orbits of *HST* time (see Table 1), are well below the halo velocity dispersion, even at $D = 100$ kpc. Therefore, PM accuracy is no impediment at all for studies of this kind. However, the small FOV of *HST* means that there are only a handful of halo stars per field. Therefore, to find the rarer stars that are at larger distances than the mean for our sample ($\langle r \rangle \sim 24$ kpc), *many* fields need to be observed.

6. CONCLUSIONS

We derive proper motions (PMs) for $N = 13$ Milky Way halo stars from three *HST*/ACS fields with long baseline (5-7 years), multi-epoch photometry. The unprecedented accuracy of these PM measurements ($\sigma_\mu \sim 0.05$ mas yr^{-1}) allows us to derive the tangential velocity ellipsoid of halo stars between $18 \lesssim r/\mathrm{kpc} \lesssim 30$. Until now, measurements of the tangential motion of halo stars have been restricted to within $D < 10$ kpc. This study is the first step towards measuring the halo velocity ellipsoid of the stellar halo beyond the solar neighborhood, independently of any assumptions regarding the underlying halo potential. We summarize our conclusions as follows:

(1) We select $N = 23$ candidate halo stars from three *HST*/ACS fields centered on M31. These stars are selected from the halo MSTO region of the CMD. The individual PMs are extracted from the multi-epoch *HST* photometry. Inspection of the proper motions of these stars shows that nine belong to M31, and one is a possible Milky Way disk star. The selected halo stars have magnitudes ranging from $21.5 < m_{F814W} < 24.5$ and are MS and/or RGB stars near the MSTO. The distances to these stars are calibrated from stellar isochrones applicable to an old, metal-poor halo population.

(2) We devise a maximum likelihood routine to derive the tangential velocity ellipsoid of these halo stars. We measure PMs for individual stars, but not their distance or radial velocities. Therefore, our determination of the velocity ellipsoid is statistical in nature. We find velocity dispersions $\sigma_b = 83^{+24}_{-16}$ km s^{-1}, $\sigma_l = 94^{+28}_{-18}$ km s^{-1} and mean streaming motion, $v_{l,0} = -75^{+28}_{-29}$ km s^{-1}. In the distance range of the halo star sample, $18 \lesssim r/\mathrm{kpc} \lesssim 30$, the Galactic velocity components closely approximate the spherical coordinate system ($v_\phi \sim -v_l$ and $v_\theta \sim v_b$).

(3) The tangential velocity components are combined with independent measures of the radial velocity dispersion ($\sigma_r \sim \sigma_{\mathrm{los}} = 105 \pm 5$ km s^{-1}) in this radial regime to estimate the velocity anisotropy of the stellar halo. We find approximate isotropy between radial and tangential velocity second moments with $\beta = 0.0^{+0.2}_{-0.4}$. This is in contrast to the strongly radial anisotropy of halo stars found in the solar neighborhood ($\beta \sim 0.7$). The increased tangential relative to radial pressure has a significant contribution from angular momentum as $\langle v_\phi \rangle \sim 70$ km s^{-1}. We note that the more tangentially biased velocity anisotropy outside of the solar neighborhood is mainly due to a *decrease* in radial pressure (from 140 to 100 km s^{-1}), rather than a significant increase in tangential pressure.

(4) The radial anisotropy profile is poorly constrained, es-

pecially at large radii. However, there is growing evidence that there may be an isotropic/tangential 'dip' in velocity anisotropy in the radial range $15 \lesssim r/\mathrm{kpc} \lesssim 25$. Intriguingly, this coincides with a break in the stellar density profile, beyond which the stellar density falls off more rapidly. These two lines of evidence suggest that there may be a shell-type structure in this radial regime. However, at present we cannot discount the influence of halo stars formed *in-situ* which may have more tangentially biased orbits than accreted stars.

REFERENCES

Beers, T. C., et al. 2012, ApJ, 746, 34
Bond, N. A., et al. 2010, ApJ, 716, 1
Bovy, J., et al. 2012, ApJ, 759, 131
Bramich, D. M., et al. 2008, MNRAS, 386, 887
Brown, T. M., Ferguson, H. C., Smith, E., Kimble, R. A., Sweigart, A. V., Renzini, A., & Rich, R. M. 2004, AJ, 127, 2738
Brown, T. M., et al. 2005, AJ, 130, 1693
—. 2006, ApJ, 652, 323
—. 2009, ApJS, 184, 152
Brown, W. R., Geller, M. J., Kenyon, S. J., & Diaferio, A. 2010, AJ, 139, 59
Bullock, J. S., & Johnston, K. V. 2005, ApJ, 635, 931
Carollo, D., et al. 2010, ApJ, 712, 692
Casetti-Dinescu, D. I., Majewski, S. R., Girard, T. M., Carlin, J. L., van Altena, W. F., Patterson, R. J., & Law, D. R. 2006, AJ, 132, 2082
Chiba, M., & Beers, T. C. 2000, AJ, 119, 2843
Deason, A. J., Belokurov, V., & Evans, N. W. 2011a, MNRAS, 411, 1480
—. 2011b, MNRAS, 416, 2903
Deason, A. J., Belokurov, V., Evans, N. W., & An, J. 2012a, MNRAS, 424, L44
Deason, A. J., et al. 2012b, MNRAS, 425, 2840
Deason, A. J., Belokurov, V., Evans, N. W., & Johnston, K. V. 2013, ApJ, 763, 113

Diemand, J., Moore, B., & Stadel, J. 2004, MNRAS, 352, 535
Font, A. S., McCarthy, I. G., Crain, R. A., Theuns, T., Schaye, J., Wiersma, R. P. C., & Dalla Vecchia, C. 2011, MNRAS, 416, 2802
Frenk, C. S., & White, S. D. M. 1980, MNRAS, 193, 295
Gould, A. 2003, ApJ, 583, 765
Jeffery, E. J., et al. 2011, AJ, 141, 171
Johnston, K. V., Sheffield, A. A., Majewski, S. R., Sharma, S., & Rocha-Pinto, H. J. 2012, ApJ, 760, 95
Kafle, P. R., Sharma, S., Lewis, G. F., & Bland-Hawthorn, J. 2012, ApJ, 761, 98
Kalirai, J. S. 2012, Nature, 486, 90
Kalirai, J. S., Guhathakurta, P., Gilbert, K. M., Reitzel, D. B., Majewski, S. R., Rich, R. M., & Cooper, M. C. 2006, ApJ, 641, 268
Kallivayalil, N., van der Marel, R. P., & Alcock, C. 2006b, ApJ, 652, 1213
Kallivayalil, N., van der Marel, R. P., Alcock, C., Axelrod, T., Cook, K. H., Drake, A. J., & Geha, M. 2006a, ApJ, 638, 772
Kepley, A. A., et al. 2007, AJ, 134, 1579
Mahmud, N., & Anderson, J. 2008, PASP, 120, 907
Majewski, S. R., Ostheimer, J. C., Rocha-Pinto, H. J., et al. 2004, ApJ, 615, 738
Martin, N. F., Ibata, R. A., & Irwin, M. 2007, ApJ, 668, L123
McCarthy, I. G., Font, A. S., Crain, R. A., Deason, A. J., Schaye, J., & Theuns, T. 2012, MNRAS, 420, 2245
McMillan, P. J. 2011, MNRAS, 414, 2446
Munn, J. A., et al. 2004, AJ, 127, 3034
Piatek, S., Pryor, C., & Olszewski, E. W. 2008, AJ, 135, 1024
Reid, M. J., et al. 2009, ApJ, 700, 137
Rocha-Pinto, H. J., Majewski, S. R., Skrutskie, M. F., Crane, J. D., & Patterson, R. J. 2004, ApJ, 615, 732
Robin, A. C., Reylé, C., Derrière, S., & Picaud, S. 2003, A&A, 409, 523
Sales, L. V., Navarro, J. F., Abadi, M. G., & Steinmetz, M. 2007, MNRAS, 379, 1464
Samurović, S., & Lalović, A. 2011, A&A, 531, 82
Schönrich, R. 2012, MNRAS, 427, 274
Schönrich, R., Asplund, M., & Casagrande, L. 2011, MNRAS, 415, 3807
Schönrich, R., Binney, J., & Dehnen, W. 2010, MNRAS, 403, 1829
Sesar, B., Jurić, M., & Ivezić, Ž. 2011, ApJ, 731, 4
Sirianni, M., et al. 2005, PASP, 117, 1049
Sirko, E., et al. 2004, AJ, 127, 914
Smith, M. C., et al. 2009, MNRAS, 399, 1223
Sohn, S. T., Anderson, J., & van der Marel, R. P. 2012a, ApJ, 753, 7
Sohn, S. T., Besla, G., van der Marel, R. P., Boylan-Kolchin, M., Majewski, S. R., & Bullock, J. S. 2012b, ApJ submitted, (arXiv:1210.6039)
van der Marel, R. P., Besla, G., Cox, T. J., Sohn, S. T., & Anderson, J. 2012b, ApJ, 753, 9
van der Marel, R. P., Fardal, M., Besla, G., Beaton, R. L., Sohn, S. T., Anderson, J., Brown, T., & Guhathakurta, P. 2012a, ApJ, 753, 8
VandenBerg, D. A., Bergbusch, P. A., & Dowler, P. D. 2006, ApJS, 162, 375
Watkins, L. L., et al. 2009, MNRAS, 398, 1757
Xue, X. X., et al. 2008, ApJ, 684, 1143
Xue, X.-X., et al. 2011, ApJ, 738, 79
Zinn, R. 1985, ApJ, 293, 424
Zolotov, A., Willman, B., Brooks, A. M., Governato, F., Brook, C. B., Hogg, D. W., Quinn, T., & Stinson, G. 2009, ApJ, 702, 1058